IEEE Photonics Journal
An IEEE Photonics Society Publication

A Dual-Channel Surface Plasmon Resonance Sensor Based on Dual-Polarized Photonic Crystal Fiber for Ultra-Wide Range and High Sensitivity of Refractive Index Detection

Volume 13, Number 1, February 2021

Haoran Wang
Weiying Rao
Jian Luo
Hongyan Fu, ***Member, IEEE***

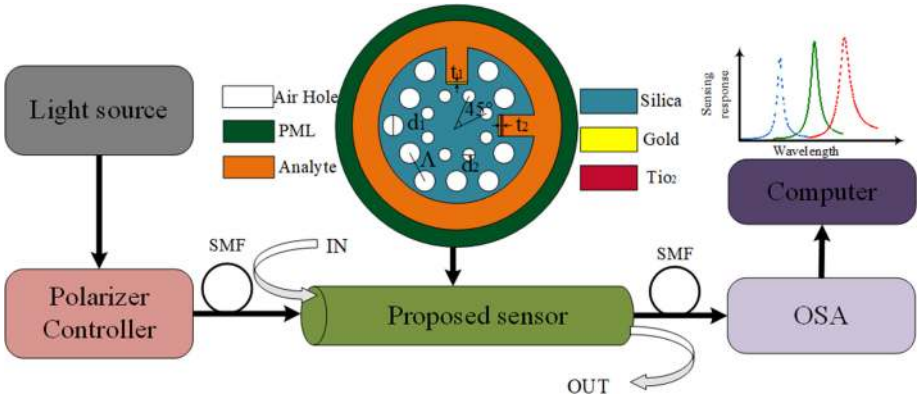

DOI: 10.1109/JPHOT.2021.3054726

A Dual-Channel Surface Plasmon Resonance Sensor Based on Dual-Polarized Photonic Crystal Fiber for Ultra-Wide Range and High Sensitivity of Refractive Index Detection

Haoran Wang, Weiying Rao, Jian Luo, and Hongyan Fu, *Member, IEEE*

Department of Electronic Engineering, School of Electronic Science and Engineering (National Model Microelectronics College), Xiamen University, Xiamen 36100, China

DOI:10.1109/JPHOT.2021.3054726

Manuscript received November 24, 2020; revised January 20, 2021; accepted January 23, 2021. Date of publication January 26, 2021; date of current version February 16, 2021. This work was supported in part by the National Natural Science Foundation of China under Grants 61975167 and 61575166 and in part by the Xiamen Science and Technology Planning Project 3502Z20183003. Corresponding author: Hongyan Fu (e-mail: fuhongyan@xmu.edu.cn).

Abstract: A surface plasmon resonance sensor based on a dual-groove photonic crystal fiber (PCF) for refractive index (RI) sensing with ultra-wide measurement range and high sensitivity is designed and theoretically investigated. The upper and right grooves of the PCF as different sensing channels are coated with Au or Au-TiO_2 compound film. The influence of the parameters on the sensing performance of the designed sensor are analyzed. Numerical results show that the maximum wavelength sensitivity (WS) of 6800 nm/RIU with a wavelength resolution of 1.47×10^{-5} RIU and maximum amplitude sensitivity (AS) of 5440 RIU^{-1} for the *x* polarization in the ultra-wide measurement range from 1.25 to 1.43 have been achieved. For *y* polarization, the proposed sensor has a maximum WS of 13200 nm/RIU and AS of 3465 RIU^{-1} in the detection range from 1.39 to 1.43. The corresponding wavelength resolution is obtained about 7.58×10^{-6} RIU. Moreover, the ultra-wide range and high sensitivity of the sensor can be flexibly adjusted by a polarization controller to meet different practical requirements. Therefore, the proposed sensor would be a suitable candidate for medical testing, bio-sensing and environmental monitoring.

Index Terms: Refractive index, photonic crystal fiber, surface plasmon resonance, ultra-wide range, high-sensitivity.

1. Introduction

The sensing technology plays an important role in many fields, such as internet of things, self-driving cars and artificial intelligence. As a novel detection technology, Surface plasmon resonance (SPR) has emerged to be one of the most promising sensing technologies due to its advantages of high sensitivity, small volume and real-time detection [1]. As a special optical phenomenon, SPR phenomenon will occur at the interface between the metal and dielectric layer when the frequency of the evanescent wave and the frequency of free electrons on the metal surface mutually coincides, which is highly capable of detecting the tiny changes of refractive index (RI) in the

surrounding environment. The sensors based on SPR have been applied in the field of water pollution monitoring, biological analyte detection and medical diagnostics, etc. [2].

Heretofore, numbers of SPR-based sensors have been proposed and extensively studied, such as optical fiber SPR sensors [3], prisms SPR sensors [4] and photonic crystal fibers (PCF) SPR sensors [5]. In particular, the combination of SPR and PCF provides researchers with novel insights and methods for developing sensors with high sensitivity and wide range. Moreover, the flexibility in structural design of PCF provides a wider space for the realization of SPR sensor.

Liu *et al.* [6] described a symmetrical dual D-shape PCF for SPR sensing with a high spectral sensitivity of 14660 nm/RIU and the sensing range is 1.36 −1.41. Wang *et al.* [7] proposed a highly sensitive SPR sensor based on D-shaped PCF, whose structure parameters are similar to the commercially available PCF. Using Indium Tin Oxide as plasmonic metal, the sensor realizes a high WS and resolution of 5200nm/RIU and 1.92×10^{-5} RIU. Dash *et al.* [8] described an aluminum-doped zinc oxide coated SPR sensor based on commercially available PCF for RI sensing. The sensor has a maximum WS of 5000nm/RIU with resolution of 2×10^{-5} RIU and AS of 167 RIU^{-1} by incorporated a microchannel into the PCF. Mahfuz *et al.* [9] reported a side-polished birefringent PCF sensor with indium tin oxide (ITO). The sensor has maximum WS as high as 17000nm/RIU, and the AS is 74 RIU^{-1}. Li *et al.* [10] designed an Ag-graphene layer-coated PCF-SPR sensor with U-shaped grooves, and the sensor exhibits the maximum wavelength sensitivity (WS) of 12600 nm/RIU as the analyte RI varies from 1.33 to 1.41. Alok *et al.* [11] demonstrated a dual core PCF sensor based on SPR, whose maximum WS reaches to 9000nm/RIU within analyte RI range from 1.33 to 1.40, and the maximum amplitude sensitivity (AS) is 726RIU^{-1} and 1085RIU^{-1} for *x* and *y* polarization, respectively. Dash *et al.* [12] introduced a PCF-based SPR by depositing metal on the outside of the PCF surface. This structure exhibits the maximum WS of 12000 nm/RIU and the sensing range is 1.33-1.40. Although these sensors have made satisfactory explorations in some aspects of sensing performance, it is still difficult to balance the WS and detection range. In particular, most of these studies frequently investigate the sensor performance in only one polarization mode. Even if both polarized modes of the proposed sensor performances are analyzed, the difference between *x* and *y* polarization is not very significant in operating wavelength windows due to the symmetry of its structure.

In this paper, we have demonstrated an SPR RI sensor based on dual-polarized PCF with tailorable high sensitivity and ultra-wide measurement range. Dual grooves of the PCF are coated with Au film and Au-TiO_2 composite film respectively as different sensing channels. This approach can reduce the material absorption losses and the core-guided light leaks at other wavelengths where there is no resonance effect. For *x* polarization, the sensor realizes a broad detection range of analyte ranging from 1.25 to 1.43 with the maximum WS of 6800 nm/RIU. Additionally, with *y* polarization, the sensor obtains a high WS and its maximum value is 13200 nm/RIU with RI ranging from 1.39 to 1.43. In addition, the maximum AS of 5440 RIU^{-1} and 3465 RIU^{-1} are obtained for *x* and *y* polarization, respectively. The influences of structural parameters on the sensing performances are investigated and discussed.

2. Model Design and Theoretical Analysis

2.1 Sensing System Design

The cross-section of the designed sensor with dual channels is depicted in Fig. 1(a). The diameter of air holes in the second layer and first layer are $d_1 = 2\ \mu$m and $d_2 = 1.2\ \mu$m, respectively. The lattice pitch of the outermost layer Λ is 3 μm. The Au film is used as the SPR material, as it has the higher resonance shift capability and is more stable in the surrounding environment. In order to obtain different sensitivity, detection range and adjust the resonant wavelength, a TiO_2 film is deposited on the top of the gold film of the right groove. In addition, the TiO_2 film can also enhance the interaction of evanescent wave with the analyte. The thicknesses of Au film and TiO_2 film are $t_1 = 0.035\ \mu$m and $t_2 = 0.06\ \mu$m, respectively. The upper groove and right U-shape grooves are used as different sensing channels to realize ultra-wide detection range and high WS.

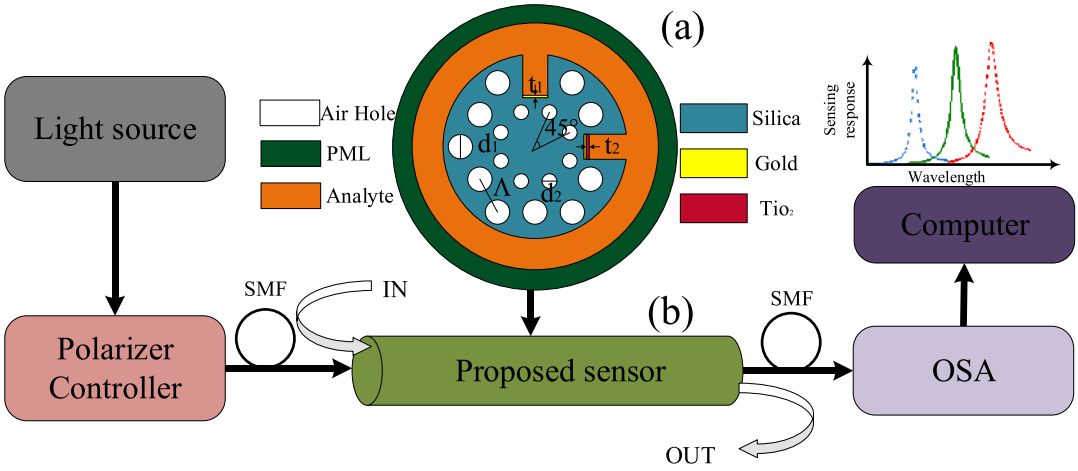

Fig. 1. (a) The cross-section of the SPR sensor (b) Sensing schematic diagram of the proposed SPR RI sensor.

The background material is fused silica, and the material dispersion is obtained by the following Sellmeier equation [13] as shown in (1):

$$n^2 = 1 + \frac{0.6961663\lambda^2}{\lambda^2 - (0.0684043)^2} + \frac{0.4079426\lambda^2}{\lambda^2 - (0.1162414)^2} + \frac{0.8974794\lambda^2}{\lambda^2 - (9.896161)^2} \tag{1}$$

where λ indicates the wavelength of the incident light and its unit is micrometer. The RI of fused silica is denoted by n, which is dependent on the λ. The complex dielectric permittivity of gold is described by Drude model [14] as the following:

$$\varepsilon_{A\mu}(T) = \varepsilon_\infty - \omega_p(T)^2/(\omega^2 + i\omega\omega_\tau(T)) \tag{2}$$

where $\varepsilon_{A\mu}(T)$ and $\omega_p(T) = 1.36 \times 10^{16}$ are the permittivity and the plasma frequency of the gold film, respectively. The dielectric constant at high frequency is described by ε_∞=9.75. ω stands for the angular frequency of the incident light which can be expressed as $\omega = 2\pi c/\lambda$, and $\omega_\tau = 1.45 \times 10^{14}$ stands for the scattering frequency of electron. Additionally, the RI of TiO_2 can be given by [15]:

$$n^2 = 5.913 + \frac{2.441 \times 10^7}{(\lambda^2 - 0.803 \times 10^7)} \tag{3}$$

The structure of proposed dual-channel sensor can be fabricated by the stack and draw technique [16]. The collapsing process of silica tubes is carried out in the lathe of Modified Chemical Vapor Deposition. In order to obtain a central void in the proposed structure, the capillaries are used to stack layer by layer in a stacking rig, and capillaries can be drawn from high-purity fused silica tubes. The U-shape groove can be made by using the side polishing method [17] and femtosecond laser micromachining technique [18]. Chemical deposition technique can be used to deposit the plasma materials on the grooves.

Fig. 1(b) illustrates the schematic diagram of a measurement setup for the proposed sensor. A linearly polarized light source is coupled to a polarization controller to generate x or y polarized light. The IN and OUT ports as the analyte flow channel can be controlled by using a pump. The transmission spectrum can be monitored by an optical spectrum analyzer (OSA).

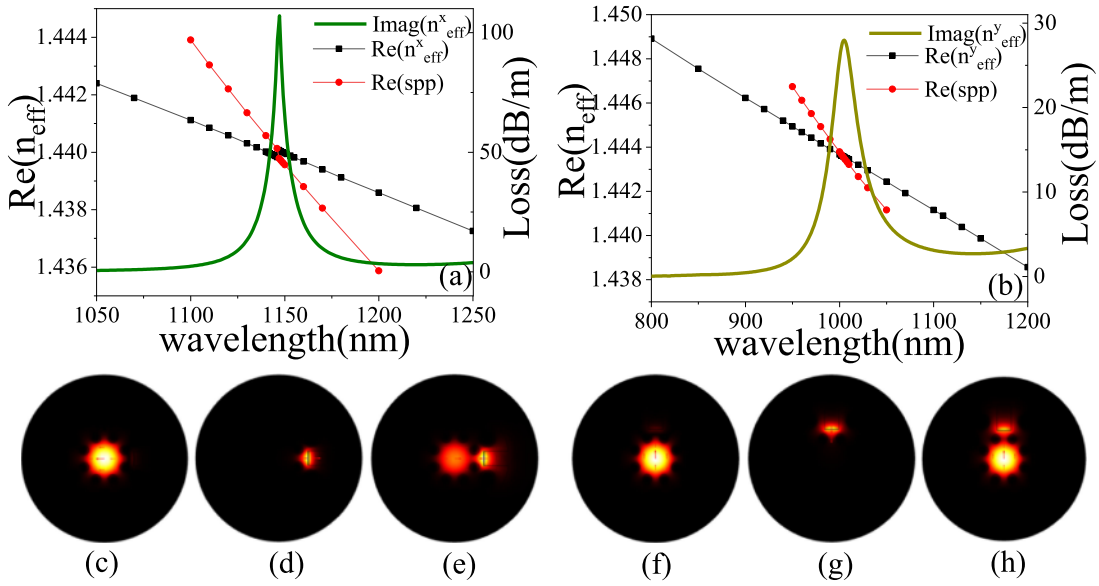

Fig. 2. The dispersion relationship between the SPP mode and (a) the *x*-pol fundamental mode (b) the *y*-pol fundamental mode, and the CL of fundamental mode, (c)–(e) and (f)–(h) optical filed distributions for x and y-polarized, respectively, at $n_a = 1.43$.

2.2 Sensing Theory

The sensing performance of the designed sensor is investigated and analyzed by finite element method (FEM) based the software of Comsol Multiphysics. The FEM is widely recognized as a very powerful technique for the analysis of optical waveguides with arbitrary shapes, index profiles, anisotropies, and nonlinearities. The intricate cross section of the PCF can be represented using many triangles of different shapes and sizes in the modal solution approach based on the FEM. In order to absorb the radiated light, the perfectly matched layer (PML) is preset at the outside of the structure. In this paper, the sensing properties of the proposed sensor can be evaluated by analyzing the confinement loss (CL), which can be defined as (4) [19], [20]:

$$\alpha_{CL}(dB/m) = \frac{20}{\ln 10} \times \frac{2\pi}{\lambda} \times \mathrm{Im}(n_{eff}) \tag{4}$$

where $\mathrm{Im}(n_{eff})$ represents the imaginary part of the effective RI and λ denotes the wavelength of incident light.

Fig. 2 shows the dispersion relations of fundamental mode and plasmonic mode. In Fig. 2(a), the black and red curves stand for the real part of effective RI of x-pol fundamental and SPP modes, respectively. The green solid line describes the variations of the CL with wavelength. Similarly, Fig. 2(b) demonstrates the real part of effective RI of *y*-pol fundamental mode (the block curve) and SPP mode (the red curve). In addition, the green brown line stands for the CL of the Y-polarized fundamental mode with different wavelength. The results of Fig. 2(a)–(b) reveal that the real part of effective RI of both SPP mode and fundamental mode decreases as the wavelength increases. Additionally, the loss of fundamental mode exhibits a sharp loss peak when the phase matching conditions are met (the intersection of dispersion relation between fundamental mode and SPP mode). The wavelength at the intersection is defined as resonance wavelength. Fig. 2(c)–(e) and (f)–(h) exhibit the optical filed distributions of the fundamental mode, SPP mode, and the coupling of fundamental mode with the SPP mode for x and y-polarized, respectively. The coupling phenomenon between fundamental modes and SPP mode can be determined and analyzed using the coupled-mode theory [21].

The sensitivity is an important parameter to evaluate the sensing performance of the sensor and can be expressed as [22], [23]:

$$WS = \frac{\Delta\lambda_{peak}}{\Delta n_a} nm/RIU \tag{5}$$

where Δn_a stands for the RI variation and $\Delta\lambda_{peak}$ represents the resonance wavelength shift. Another important parameter is resolution of the sensor which can be calculated with ignoring the instrumental noise by [24]:

$$R = \frac{\Delta n_a \bullet \Delta\lambda_{min}}{\Delta\lambda_{peak}} \tag{6}$$

where $\Delta\lambda_{min}$=0.1 nm is the minimum wavelength resolution. In addition, AS is another significant parameter to interpret the sensing performance of the sensor. By using amplitude monitoring method, an analyte can be detected at a single wavelength. Compared to wavelength interrogation method, measurement of AS is easier than wavelength tracking. The AS can be obtained by (7) [25]:

$$S_A(\lambda) = -\frac{1}{\alpha(\lambda, n_a)} \frac{\delta\alpha(\lambda, n_a)}{\delta n_a} (RIU^{-1}) \tag{7}$$

where $\delta\alpha(\lambda, n_a)$ represents the difference between two loss spectra due to two adjacent analyte RI, $\alpha(\lambda, n_a)$ denotes the AS when analyte RI is n_a. The change of adjacent analyte RI is described byδn_a.

3. Simulation and Results

3.1 Effect of Pitch on Sensing Performance

The pitch (Λ) variation effect on the sensing performance CL and AS is investigated, which is shown in Fig. 3. From Fig. 3 (a-b) it is obvious that the loss depth is significantly increased and the loss peak has a blue shift as the scaling up of Λ size. Fig. 3(c)–(d) illustrates the effect of pitch variation on the AS for *x* and *y* polarized modes. The maximum ASs are obtained about 5825, 5439 and 4914 RIU^{-1} and the WSs are 7400, 6800 and 6200 nm/RIU with the Λ from 2.9 to 3.1 μm when considering the *x*-pol mode. With *y*-pol mode, the AS peaks appeared about 3148, 3464 and 3712 RIU^{-1} and the theoretical WSs are 15400, 13200 and 11800 nm/RIU. Considering both the WS and AS, the optimized pitch is to be $\Lambda = 3$ μm.

3.2 Effect of d_1 and d_2 on Sensing Performance

In order to obtain the optimum structural parameters, the effects of air hole diameters (d_1 and d_2) variations on the sensor's performance have also been also investigated. Fig. 4(a) and (b) illustrate the influence of d_1 from 1.9 to 2.1 μm on CL at $n_a = 1.42$ and 1.43 for *x* and *y* polarized modes, respectively, while other parameters are $\Lambda = 3$ μm, $d_2 = 1.2$ μm, $t_1 = 0.035$ μm and $t_2 = 0.06$ μm. One can see that, the variation diameter d_1 changes the loss characteristics (loss depth and resonance wavelength shift). Nevertheless, the variation is not very significant. Fig. 4(c)–(d) show that maximum ASs are about 4719, 5439 and 5849 RIU^{-1} for *x*-pol mode, while the WSs are 7000, 6800 and 6600 nm/RIU, respectively. Considering *y*–pol mode, the obtained maximum AS are about 3509, 3464 and 3431 RIU^{-1} respectively and the WSs are 13400, 13200 and 13000 nm/RIU, respectively. The optimized d_1 is selected to be $d_1 = 2$ μm because we make a balance between the WS and AS.

Similarly, Fig. 5 indicates that the influence of d_2 from 1.15 μm to 1.25 μm on the sensor's performance when $\Lambda = 3$ μm, $d_1 = 2$ μm, $t_1 = 0.035$ μm and $t_2 = 0.06$ μm. One can see from Fig. 5(a)–(b) that, the variation of d_2 has an effect on the loss characteristics. For d_2 of 1.15 μm, 1.20 μm, and 1.25 μm, the corresponding maximum ASs of 3914, 5439 and 6173 RIU^{-1} for *x*-pol mode and 3446, 3464 and 3510 RIU^{-1} for *y*-pol mode at $n_a = 1.42$ have been achieved, which

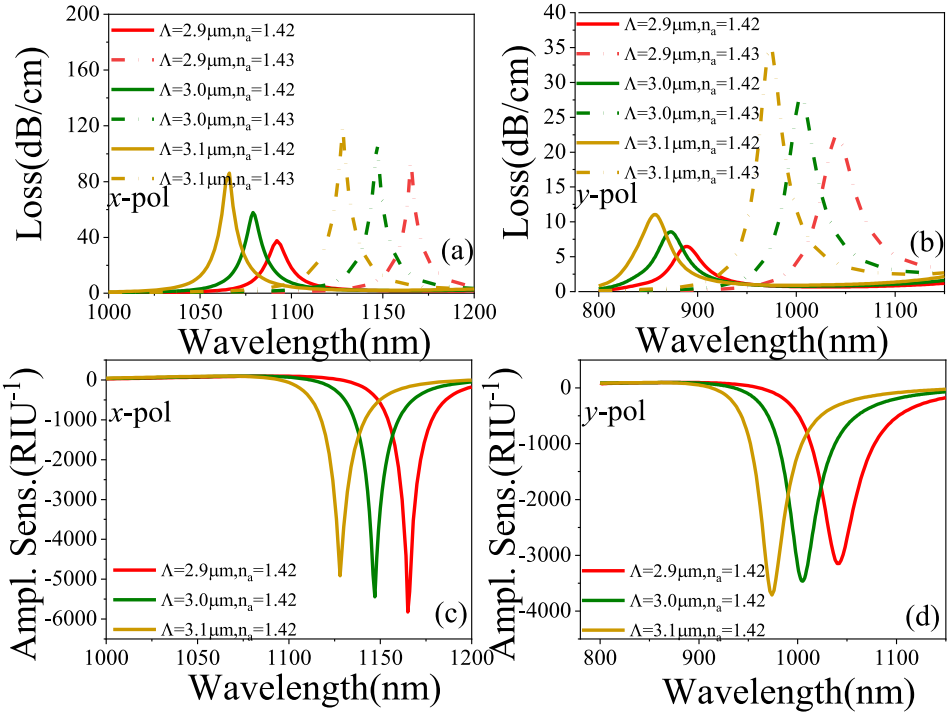

Fig. 3. CL(a)–(b), AS (c)–(d) with the variation of Λ.

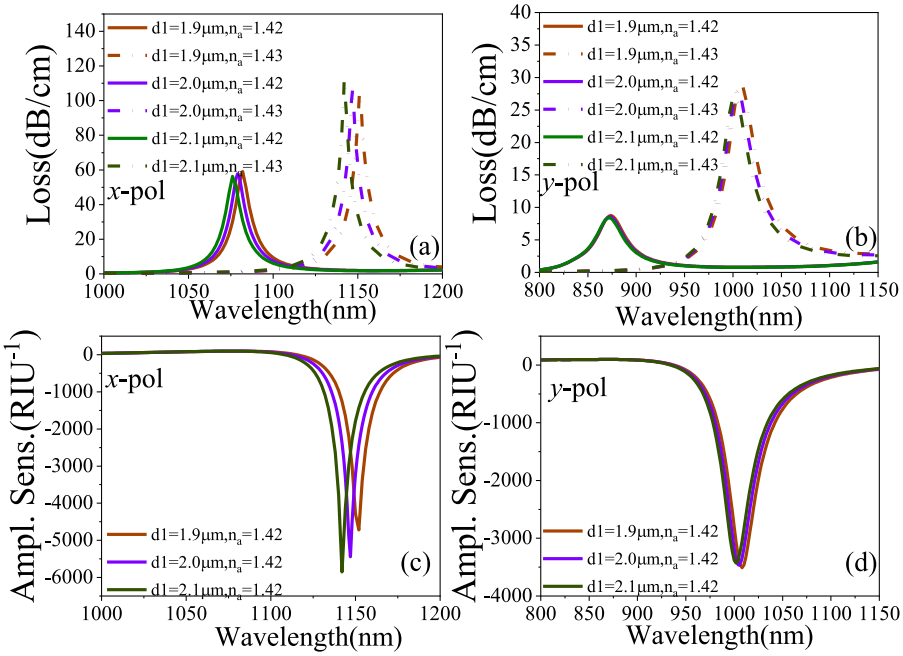

Fig. 4. CL (a)–(b) and AS (c)–(d) of the proposed sensor with variation of d_1.

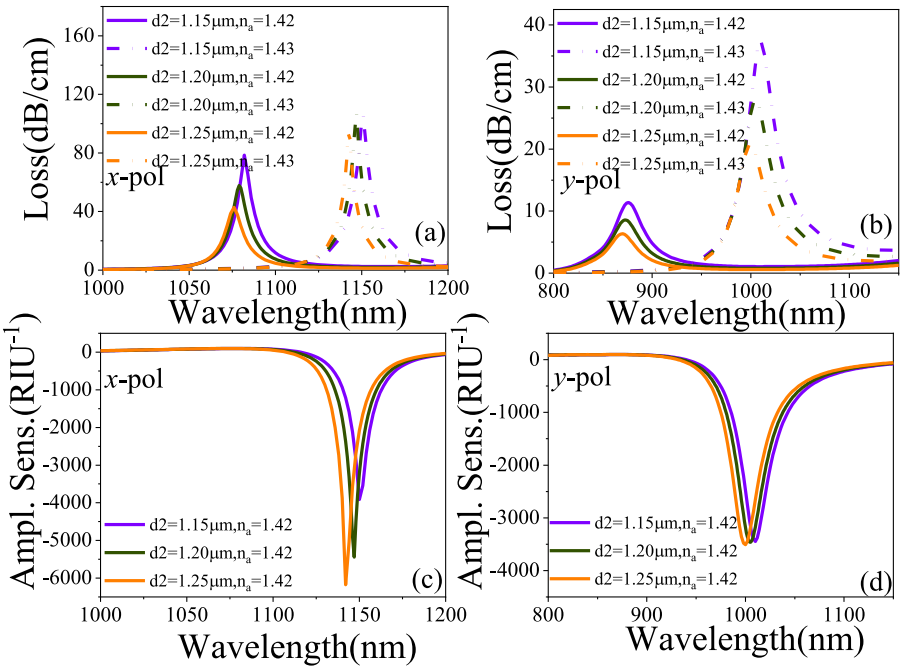

Fig. 5. CL (a)–(b) and AS (c)–(d) of the proposed sensor with variation of d_2.

is illustrated in Fig. 5(c)–(d). The WSs are observed about 6800, 6800 and 6600 nm/RIU for *x*-pol mode and 13400,13200 and 13000 nm/RIU for *y*-pol mode, which is not very significant. The optimized pitch is to be $d_2 = 1.2\ \mu$m through considering both the WS and AS.

3.3 Effect of Au and TiO_2 Film Thicknesses on Sensing Performance

The thicknesses of Au film and TiO_2 film have important impact on the sensor's CL and AS, which is depicted in Fig. 6. As can be seen from Fig. 6(a1)–(a2), it is obvious that the CL peak has a significant red shift and the loss depth is significantly decreased as the increment of Au film thickness from 35 to 45 nm. From Fig. 6(a3), it is evident that a sharp loss peak and maximum AS are achieved when the thickness of Au is set at 35 nm. Additionally, making a 35 nm gold layer is easier than a thinner gold layer. Therefore, the selected optimum Au film thickness is 35 nm. Fig. 6(b1)–(b2) indicates that the loss depth increases with an increase of thickness of TiO_2 layer from 50 to 70 nm for *x*-pol mode and *y*-pol mode. It is notable that, since the TiO_2 film is only deposited in horizontal channel, the loss characteristics of *y*-pol mode remain unchanged with the changes of TiO_2 film thickness. Considering *x* -polarized mode, the ASs about 5950, 5439 and 4549 RIU^{-1} have been obtained with the increase of TiO_2 film thickness. The corresponding WSs are 7400, 6800 and 6200 nm/RIU. However, it is worthwhile to note that the loss peak broadening with the decrease of TiO_2 film's thickness. Considering the WS, AS, and loss peak broadening, 60 nm is chosen as an optimal TiO_2 thickness.

3.4 Results and Discussions

From simulation results above, the CL characteristics of the proposed sensor using optimized parameters have been calculated for different n_a. Fig. 7(a) shows the confinement loss of the *x*-polarized fundamental mode with RI variation ranging from 1.33 to 1.43. It can be seen that the resonance wavelength moves to a longer wavelength as the RI of analyte increases.

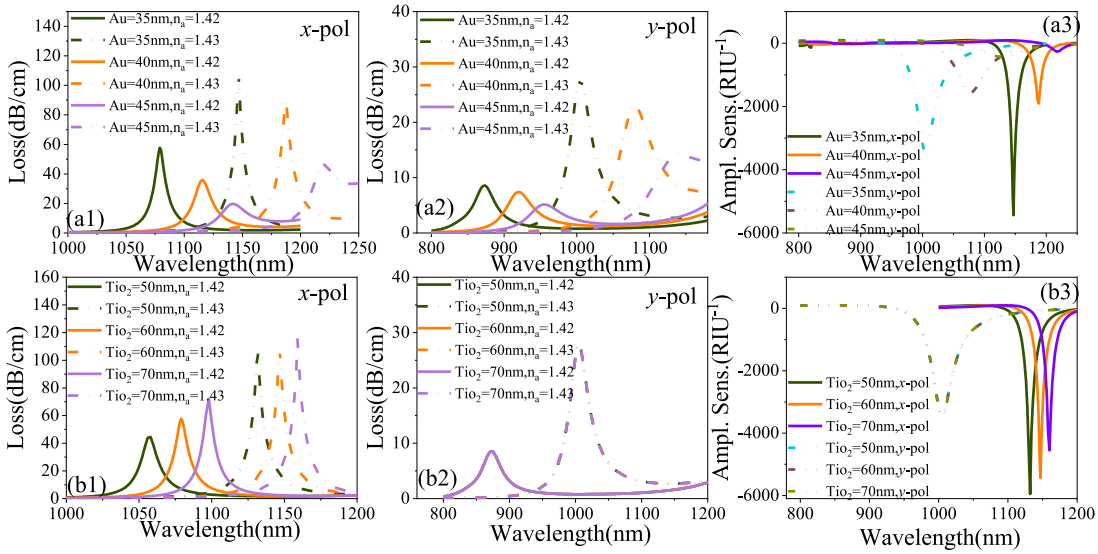

Fig. 6. CL (a1)–(a2), AS (a3) and CL (b1)–(b2), AS (b3) for thickness variations of Au and TiO_2 films.

The relationship between analyte's RI and the resonant wavelength for *x*-polarized fundamental mode is plotted in Fig. 7(b). The corresponding polynomial equation is $\lambda = 12714.88{n_a}^2 - 31885.87n_a + 20715.51$ and then, taking the derivative of the polynomial equation, we can obtain the spectral sensitivity $\lambda_s = 25429.76n_a - 31885.87$. Based on (5) and (6), in the sensing range from 1.25 to 1.43, the maximum WS is 6800 nm/RIU with a resolution of 1.47×10^{-5} RIU. For *x*-polarized fundamental mode, the designed sensor achieves a wider range of RI detection with high sensitivity.

The loss of *y*-polarized fundamental mode is investigated and the results as shown in Fig. 7(c). Fig. 7(d) depicts the relationship between the resonance wavelength and different analyte's RI. The corresponding polynomial equation is $\lambda = 151428.57{n_a}^2 - 419308.57n_a + 290956.66$. $\lambda_s = 302857.14n_a - 419308.57$ is the spectral sensitivity which can be calculated by taking the derivative of the polynomial equation. The results show that the WS of the proposed sensor is obtained to be as high as 13200nm/RIU within the sensing range from 1.39-1.43 and the corresponding resolution is 7.58×10^{-6} RIU.

Furthermore, the AS of both *x* and *y*-pol mode is also calculated by using (7). As is depicted in Fig. 8(a), the AS of both *x* and *y*-pol mode goes higher with the increasing n_a. This is because that the interaction of the SPP and the core fundamental mode gets stronger at higher analyte's RI regime, and thus the AS increases dramatically. For *x*-pol mode, the minimum and maximum AS are calculated to be 148.54 RIU^{-1} and 5439.58 RIU^{-1} at $n_a = 1.25$ and 1.42, respectively. For *y*-pol mode, the lowest AS is obtained about 764.03 RIU^{-1} at $n_a = 1.39$, while the maximum AS of 3464.67 RIU^{-1} is achieved when $n_a = 1.43$. Besides, by varying n_a from 1.39-1.43, *x*-pol mode exhibits better AS than *y*-pol mode.

The influence of variation of structural parameters on the spectral response are investigated when $n_a = 1.43$, which is shown in Fig. 9(a)–(e). It is obvious that the spectral response can be precisely regulated by changing the structural parameters. This improves the design flexibility of the proposed sensor.

The signal-to-noise ratio is also an important for the sensing performance of the proposed sensor and the figure of merit (FOM) can be used to characterize this characteristic. FOM can be defined as (8) [26]:

$$FOM = \frac{Sensitivity(nm/RIU)}{FWHM(nm)} \tag{8}$$

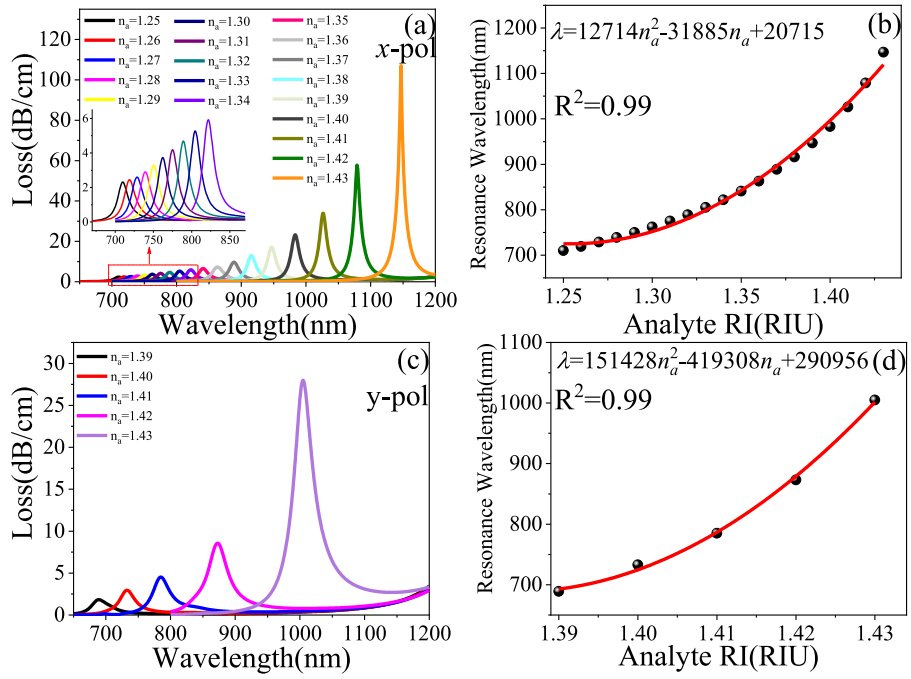

Fig. 7. CL for (a) *x*-pol and (c) *y*-pol mode, and resonance wavelength for (b) *x*-pol and (d) *y*-pol mode with variation of analyte's n_a from 1.25–1.43, while $\Lambda = 3\ \mu$m, d1 $= 2\ \mu$m, d2 $= 1.2\ \mu$m, $t_{Au} = 35$ nm, $t_{TiO2} = 60$ nm.

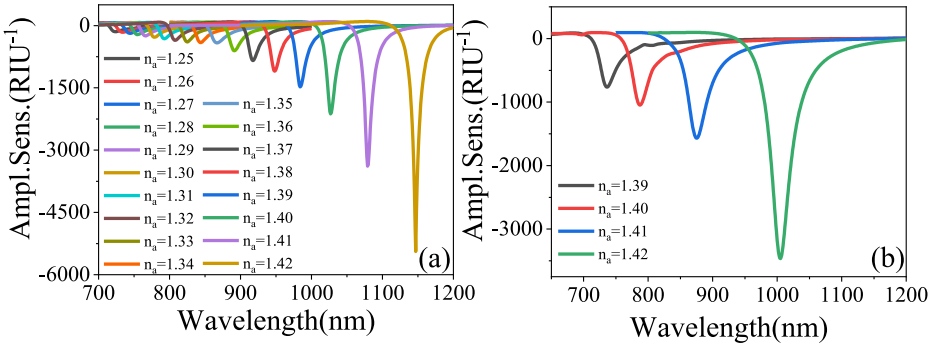

Fig. 8. AS for (a) *x*-pol and (b) *y*-pol mode with variations of analyte's n_a from 1.25–1.43.

where the FWHM represents full width at half maximum of CL. Fig. 9(f) shows the FOM when varying n_a from 1.25 to 1.43. The results show that the maximum FOMs of 527 and 363 RIU^{-1} are achieved by using (8) for *x* and *y* polarized modes when $n_a = 1.43$. Using a gold film coated groove can effectively reduce the material absorption losses and the core-guided light leaks at other wavelengths where there is no resonance effect, so the proposed sensor exhibits higher FOM. A higher FOM means a better quality performance.

On the basis of all the above investigations, it comes to a conclusion that the sensor realizes ultra-wide range, high WS and amplitude sensitivity by using different polarized modes. Moreover, different sensing characteristics can be flexibly switched through a polarization controller to meet application requirements. The performance comparison of the existing sensors and our proposed

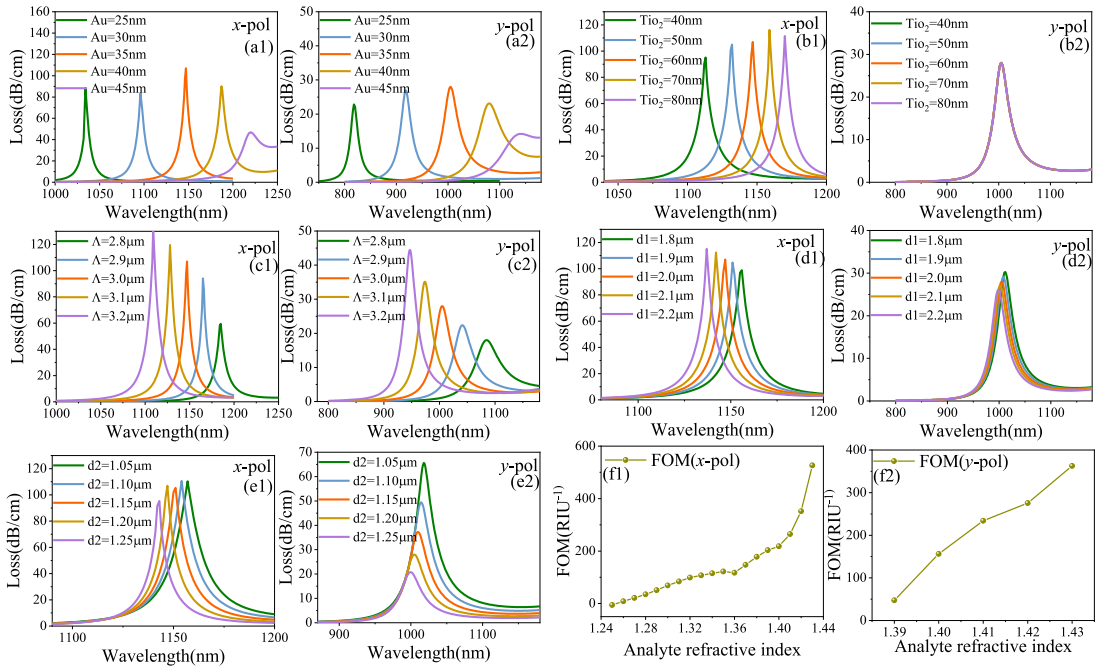

Fig. 9. The loss spectra for different value of (a) t_1 (Au film's thickness), (b) t_2 (TiO_2 film's thickness), (c) Λ (pitch), (d) d_1, (e) d_2. (f) FOM of the sensor with variations of analyte's RI using optimized sensor's parameters.

TABLE 1
Comparison of Sensing Performance of the Existing Sensors and Our Proposed Sensor

Ref	Measured parameters	Dynamic range	sensitivity (nm/RIU)	resolution	AS(RIU^{-1})
[9]	RI	1.33-1.40	12000	8.33×10^{-6}	1656
[27]	RI	1.33-1.43	9800	2.2×10^{-6}	1086
[28]	RI	1.36-1.38	3340	5.98×10^{-6}	69
[29]	RI	1.40-1.43	15180	5.68×10^{-6}	498
[30]	RI	1.0-1.6	2275	4.396×10^{-5}	88
This work	RI	1.25-1.43(*x*-pol)	6800	1.47×10^{-5}	5440
		1.39-1.43(*y*-pol)	13200	7.58×10^{-6}	3465

sensor are presented in Table 1, which shows that the sensing performance of the proposed sensor exhibits very competitive performance.

4. Conclusion

In this paper, we designed and analyzed a dual-channel SPR sensor based on PCF for RI detection, which enjoys ultra-wide range and high sensitivity. The sensing performance of the proposed sensor with different designing parameters has been investigated by using FEM and PML. Different sensing channels are designed based on the polarization filtering of PCF to obtain different sensing performance. The simulation results show that the widest RI detection range of the proposed sensor is 1.25–1.43 with a maximum AS of 5440 RIU^{-1} and the maximum WS is 13200 nm/RIU. Owing to the remarkable sensing performance, the proposed sensor can be a favorable candidate in medical testing, biomedicine and biochemical fields.

References

[1] M. S. Islam *et al.*, "Dual-polarized highly sensitive plasmonic sensor in the visible to near-IR spectrum," *Opt. Exp.*, vol. 26, no. 23, pp. 30347–30361, Nov. 2018.

[2] A. X. Xiao *et al.*, "An optical microfiber biosensor for CEACAM5 detection in serum: Sensitization by a nanosphere interface," *Acs Appl. Materials Interfaces*, vol. 12, no. 1, pp. 1799–1805, Jan. 2020.

[3] H. Y. Fu, S. W. Zhang, H. Chen, and J. Weng, "Graphene enhances the sensitivity of fiber-optic surface plasmon resonance biosensor," *IEEE Sensors J.*, vol. 15, no. 10, pp. 5478–5482, Oct. 2015.

[4] E. Kretschmann and H. Raether, "Radiative decay of non radiative surface plasmons excited by light," *Zeitschrift Fur Naturforschung A*, vol. 23, no. 12, pp. 2135–2136, 1968.

[5] E. Haque, S. Mahmuda, M. A. Hossein, N. H. Hai, Y. Namihira, and F. Ahmed, "Highly sensitive dual-core PCF based plasmonic refractive index sensor for low refractive index detection," *IEEE Photon. J.*, vol. 11, no. 5, Oct. 2019, Art. no. 7905309.

[6] C. Liu *et al.*, "Symmetrical dual D-shape photonic crystal fibers for surface plasmon resonance sensing," *Opt. Exp.*, vol. 26, no. 7, pp. 9039–9049, Apr. 2018.

[7] G. Y. Wang *et al.*, "Highly sensitive D-shaped photonic crystal fiber biological sensors based on surface plasmon resonance," *Opt. Quantum Electron.*, vol. 48, no. 1, p. 46, Jan. 2016.

[8] J. N. Dash, R. Das, and R. Jha, "AZO coated microchannel incorporated PCF-Based SPR sensor: A numerical analysis," *IEEE Photon. Technol. Lett.*, vol. 30, no. 11, pp. 1032–1035, Jun. 2018.

[9] M. Al Mahfuz *et al.*, "Highly sensitive photonic crystal fiber plasmonic biosensor: Design and analysis," *Opt. Mater.*, vol. 90, pp. 315–321, Apr. 2019.

[10] T. S. Li *et al.*, "A refractive index sensor based on H-Shaped photonic crystal fibers coated with ag-graphene layers," *Sensors*, vol. 20, no. 3, p. 741, Feb. 2020.

[11] A. K. Paul, A. K. Sarkar, A. B. S. Rahman, and A. Khaleque, "Twin core photonic crystal fiber plasmonic refractive index sensor," *IEEE Sensors J.*, vol. 18, no. 14, pp. 5761–5769, Jul. 2018.

[12] J. N. Dash and R. Jha, "Highly sensitive side-polished birefringent PCF-Based SPR sensor in near IR," *Plasmonics,* vol. 11, no. 6, pp. 1505–1509, Dec. 2016.

[13] G. Ghosh, M. Endo, and T. Iwasaki. "Temperature-dependent sellmeier coefficients and chromatic dispersions for some optical fiber glasses," *J. Lightw. Technol.*, vol. 12, no. 8, pp. 1338–1342, Aug. 1994.

[14] A. Vial *et al.*, "Improved analytical fit of gold dispersion: Application to the modeling of extinction spectra with a finite-difference time-domain method," *Phys. Rev. B.*, vol. 71, no. 8, p. 85416, Feb. 2005.

[15] A. A. Rifat *et al.*, "Highly sensitive multi-core flat fiber surface plasmon resonance refractive index sensor," *Opt. Exp.*, vol. 24, no. 3, pp. 2485–2495, Feb. 2016.

[16] P. Russell, "Photonic crystal fibers," *Science*, vol. 299, no. 5605, pp. 358–362, Jan. 2003.

[17] S. Chu *et al.*, "Influence of the sub-peak of secondary surface plasmon resonance onto the sensing performance of a d-shaped photonic crystal fibre sensor," *IEEE Sensors J.,* vol. 21, no. 1, pp. 33–42, Jan. 2021.

[18] A. van Brakel *et al.*, "Micro-channels machined in microstructured optical fibers by femtosecond laser," *Opt. Exp.*, vol. 15, no. 14, pp. 8731–8736, Jul. 2007.

[19] Z. H. Zhang *et al.*, "Dependence of leaky mode coupling on loss in photonic crystal fiber with hybrid cladding," *Opt. Exp.*, vol. 16, no. 3, pp. 1915–1922, Feb. 2008.

[20] M. Al Mahfuz, M. A. Hossain, E. Haque, N. H. Hai, Y. Namihira, and F. Ahmed, "Dual-Core photonic crystal fiber-based plasmonic RI sensor in the visible to near-IR operating band," *IEEE Sensors J.*, vol. 20, no. 14, pp. 7692–7700, Jul. 2020.

[21] B. B. Shuai *et al.*, "A multi-core holey fiber based plasmonic sensor with large detection range and high linearity," *Opt. Exp.*, vol. 20, no. 6, pp. 5974–5986, Mar. 2012.

[22] X. Chen, L. Xia, and C. Li, "Surface plasmon resonance sensor based on a novel D-shaped photonic crystal fiber for low refractive index detection," *IEEE Photon. J.*, vol. 10, no. 1, Feb. 2018, Art. no. 6800709.

[23] A. Hassani and M. Skorobogatiy, "Photonic crystal fiber-based plasmonic sensors for the detection of biolayer thickness," *J. Opt. Soc. Amer. B-Opt. Phys.*, vol. 26, no. 8, pp. 1550–1557, Aug. 2009.

[24] M. Hautakorpi, M. Mattinen, and H. Ludvigsen, "Surface-plasmon-resonance sensor based on three-hole microstructured optical fiber," *Opt. Exp.*, vol. 16, no. 12, pp. 8427–8432, Jun. 2008.

[25] E. Haque, M. A. Hossain, F. Ahmed, and Y. Namihira, "Surface plasmon resonance sensor based on modified D-shaped photonic crystal fiber for wider range of refractive index detection," *IEEE Sensors J.*, vol. 18, no. 20, pp. 8287–8293, Oct. 2018.

[26] M. Momtaj *et al.*, "Open-channel-based dual-core D-shaped photonic crystal fiber plasmonic biosensor," *Appl. Opt.*, vol. 59, no. 28, pp. 8856–8865, Oct. 2020.

[27] A. A. Rifat, R. Ahmed, G. A. Mahdiraji, and F. R. M. Adikan, "Highly sensitive D-shaped photonic crystal fiber-based plasmonic biosensor in visible to Near-IR," *IEEE Sensors J.*, vol. 17, no. 9, pp. 2776–2783, May 2017.

[28] J. J. Lu *et al.*, "D-shaped photonic crystal fiber plasmonic refractive index sensor based on gold grating," *Appl. Opt.*, vol. 57, no. 19, pp. 5268–5272, Jul. 2018.

[29] M. Liu *et al.*, "High-sensitivity birefringent and single-layer coating photonic crystal fiber biosensor based on surface plasmon resonance," *Appl. Opt.*, vol. 57, no. 8, pp. 1883–1886, Mar. 2018.

[30] Y. Guo *et al.*, "Amphibious sensor of temperature and refractive index based on D-shaped photonic crystal fibre filled with liquid crystal," *Liq. Cryst.*, vol. 47, no. 6, pp. 882–894, May 2020.